

The Sea Spray Contribution to Sensible Heat Flux

DAVID H. RICHTER* AND PETER P. SULLIVAN

National Center for Atmospheric Research, Boulder, Colorado

(Manuscript received 3 July 2013, in final form 15 October 2013)

ABSTRACT

Direct numerical simulations (DNS) of turbulent Couette flow are combined with Lagrangian point-particle tracking to investigate the effects of a dispersed phase on bulk passive heat transport when the two phases can exchange both momentum and sensible heat. The idealized setup allows a fixed number of particles, without the influence of gravity, to be transported by carrier-phase motions across the mean velocity and temperature gradients that exist between the solid boundaries of turbulent Couette flow. In this way, the setup serves as a model of spray in a shear-dominated layer in the immediate vicinity of the water surface and provides insight into the ability of spray to enhance sensible heat fluxes. The authors find that the dispersed phase contributes a relatively large amount of vertical heat transport and increases the total heat flux across the domain by 25% or greater. Particles that accumulate in regions associated with wall-normal ejections efficiently carry heat across the channel. Furthermore, the authors find that the relative contribution of the dispersed-phase heat flux becomes larger with Reynolds number, suggesting an importance at atmospheric scales.

1. Introduction

For predicting the intensity of tropical cyclones, detailed knowledge of the exchanges of heat, moisture, and momentum at the air–sea interface is essential. While the flux of latent and sensible heat from the ocean provides fuel for the storm, drag on the surface can act to weaken it, and thus a better understanding of the balance between these processes is required if hurricane intensity forecasts are to be improved (Emanuel 1995; NOAA Science Advisory Board 2006). Because of the extreme conditions and the practical difficulties associated with making accurate measurements within the high-wind boundary layer, direct observations of the fluxes of heat, moisture, and momentum are rare. For this reason, other efforts, such as numerical and theoretical modeling, are needed to improve the current understanding of near-surface physical processes.

In a recent study, we use direct numerical simulations (DNS; i.e., all scales of turbulent motion are resolved) of turbulent Couette flow coupled with Lagrangian point

particles to investigate the changes inertial particles induce in momentum flux (Richter and Sullivan 2013b). By altering near-surface turbulent motions, the presence of a dispersed phase such as sea spray may, at sufficiently high concentrations, change the turbulent flux of momentum. It is found, however, that momentum carried by the dispersed phase becomes a significant fraction of the total momentum flux to the surface, compensating for losses in the turbulent flux. What results is a total flux of momentum that is nearly unchanged despite an observed reduction in the turbulent flux. In practice, this implies that eddy flux measurements of the turbulent flux $\rho\langle u'w' \rangle$ taken in regions of high spray concentration may underestimate the total flux of momentum. Studies such as that by Donelan et al. (2004) indicate that, for the concentrations of spray present in their experiments, the contribution to momentum transport from the dispersed phase is small since both direct and indirect measurements of the water surface stress agree.

The process of the dispersed-phase momentum transport compensating for losses in the turbulent flux is an illustration of the ideas proposed by Andreas (2004), where the author treats the momentum flux problem as a closed system. Since inertial spray droplets are accelerated by the wind (extracting horizontal momentum from the air), then plunge back into the water (along with the horizontal momentum gained from the air), the ability of spray to directly change the total transfer

* Current affiliation: Department of Civil and Environmental Engineering and Earth Sciences, University of Notre Dame, Notre Dame, Indiana.

Corresponding author address: David Richter, University of Notre Dame, 156 Fitzpatrick Hall, Notre Dame, IN 45665.
E-mail: david.richter.26@nd.edu

of momentum to the ocean surface is seemingly small, which is in agreement with the findings of our previous work (Richter and Sullivan 2013b). Only through indirect effects, such as modifying the near-surface atmospheric stability through thermodynamic exchange (Bianco et al. 2011) or a disruption of the turbulent energy cascade, can spray produce significant modifications to the total momentum flux.

While the momentum flux balance near the surface is a closed system with regard to sea spray, the fluxes of latent and sensible heat, on the other hand, are not. In principle, therefore, spray can modify the exchange of these quantities. Fairall et al. (1994) use a bulk model to estimate the spray-mediated fluxes of sensible and latent heat, and find that these fluxes become comparable to the interfacial fluxes (i.e., fluxes carried by turbulent air motions) at wind speeds above roughly 20 m s^{-1} . They also suggest that the total latent heat flux measured above the droplet layer is enhanced, while the sensible heat flux is diminished. Makin (1998) uses a one-dimensional turbulence model of the horizontally averaged surface layer, with explicit representation of spray-mediated source–sink functions within the moisture and heat transport equations.

Generally, the addition of spray can significantly alter the total fluxes of sensible heat and moisture. The presence of spray is seen to decrease the flux of one of these quantities at the expense of the other, and this depends strongly on atmospheric stability. As in Fairall et al. (1994), spray-mediated fluxes become comparable to the interfacial fluxes at winds of 25 m s^{-1} . More recently, Bianco et al. (2011) simultaneously model the heat, moisture, and momentum flux contributions from spray within a one-dimensional surface layer model and find enhancements of sensible and latent heat flux at sufficiently high wind speeds, with a complex interplay between near-surface stratification effects (due to cooling of the air during the droplet evaporation process) and the additional sensible heat supplied by the spray droplets.

Andreas and Emanuel (2001) point out, using the analysis of Emanuel (1995), that the net enthalpy flux (and its relative effect compared to the momentum flux) is the quantity of interest when considering tropical storm intensity, rather than the individual fluxes of sensible and latent heat. Since evaporating droplets extract heat from the surrounding air (thus resulting in no net enthalpy flux), the work of Andreas and Emanuel (2001) emphasizes the need for understanding the additional enthalpy flux due to reentrant spray–droplets that exchange their sensible heat but fall back into the water before evaporating. They find that incorporating this additional enthalpy flux into the axisymmetric tropical cyclone model of Emanuel (1995) leads to enhanced storm intensity.

Bao et al. (2011) take a slightly different approach and parameterize the effects of spray on the momentum and sensible and latent heat fluxes from the surface within a hurricane model by adjusting the stability length in Monin–Obukhov similarity theory to account for spray effects on near-surface stratification. They predict an increase in the enthalpy transfer coefficient C_K at winds greater than $30\text{--}40 \text{ m s}^{-1}$ due to spray and demonstrate that the inclusion of their observed changes in surface momentum and enthalpy flux acts to substantially intensify a simulated tropical cyclone.

With similar results, Andreas (2011) uses the bulk flux algorithm developed in Andreas et al. (2008) and Andreas (2010), which is based on the premise that interfacial and spray-mediated heat exchanges scale differently with wind speed, to show that spray contributions can enhance enthalpy fluxes at winds higher than roughly 20 m s^{-1} . Even below this value of wind speed, he suggests that spray still plays a significant role in total heat transfer from the surface, compensating for the gap that exists between theoretically predicted interfacial heat fluxes (without spray) and those measured in the field (e.g., DeCosmo et al. 1996).

All of these modeling studies attempt to estimate the total amount of extra heat added to the atmosphere by spray. Despite the differences in the model details and assumptions, they all indicate that spray enhances the enthalpy flux at sufficiently high winds, beyond that predicted without spray. This conclusion, however, increasingly seems to be in contradiction with the few existing observations.

The Humidity Exchange over the Sea (HEXOS) measurements of vapor and sensible heat flux (DeCosmo et al. 1996) show no obvious dependence of the exchange coefficients of sensible and latent heat (C_H and C_E , respectively) with wind speed up to roughly 20 m s^{-1} . These data, however, are used in conjunction with a microphysical model and the Tropical Ocean–Global Atmosphere Coupled Ocean–Atmosphere Response Experiment (TOGA COARE) version 2.6 bulk-flux algorithm (Fairall et al. 1996) to determine the relative contributions from interfacial and spray-mediated transfer (Andreas and DeCosmo 2002; Andreas et al. 2008). Andreas and DeCosmo (2002) show that the lack of wind speed dependence of the bulk moisture and sensible heat transfer coefficients does not imply the absence of spray effects at these wind speeds; rather, they conclude that the HEXOS data show that spray contributes up to 40% of the total latent heat flux at wind speeds as low as $15\text{--}18 \text{ m s}^{-1}$.

Fluxes measured directly from aircraft in the Coupled Boundary Layer Air–Sea Transfer (CBLAST) experiment (Black et al. 2007) also indicate that transfer coefficients of sensible (Zhang et al. 2008) and latent

(Drennan et al. 2007) heat are independent of wind speed, up to roughly 30 m s^{-1} . In his modeling study, however, Andreas (2011) shows that a wind speed of 30 m s^{-1} is at the lower boundary of where spray begins to cause an upward deviation of C_K , suggesting that these measurements were not made at sufficiently high wind speeds to observe the effects of spray on enthalpy transfer. Furthermore, Andreas (2011) argues that when considering the scatter in the CBLAST measurements, the lack of wind speed dependence is not inconsistent with the theory that spray enhances the fluxes of sensible heat and enthalpy.

Recently, Bell et al. (2012) construct axisymmetric angular momentum and total energy budgets of Hurricanes Fabien and Isabel using data collected during the CBLAST program. With these budgets, they are able to indirectly compute surface enthalpy and momentum fluxes in regions of very high winds, albeit with significant uncertainty in the final values. They find no statistical dependence of C_K with wind speed out to 72 m s^{-1} , and they conclude that the spray (which would be implicitly included in their budget analysis) does not change C_K at high winds. This lack of wind speed dependence on C_K is corroborated by laboratory measurements (Haus et al. 2010; Jeong et al. 2012), where enthalpy flux measurements are made calorimetrically (i.e., monitoring changes in water tank temperature at various wind speeds). Up to 10-m wind speeds of 38 m s^{-1} , and assuming scalability up to atmospheric scales, their values of C_K remain constant, suggesting that even at wind speeds exceeding 30 m s^{-1} , increased spray mass loading does not enhance the net enthalpy flux from the surface. It should be noted that in the analyses done by Bell et al. (2012), Haus et al. (2010), and Jeong et al. (2012), as well as any other direct or indirect measurements of the air-sea interface, it is impossible to determine the individual contributions from spray-mediated and interfacial fluxes.

A discrepancy, therefore, seems to be forming between measurements and the predictions of high-wind surface-layer models regarding the role of spray on moisture, sensible heat, and enthalpy fluxes. Our current goal, therefore, is to use DNS of turbulent Couette flow, coupled with Lagrangian point-particle tracking, to understand the fundamentals of how a dispersed phase can modify sensible heat fluxes in an idealized framework. This is an extension of our previous work (Richter and Sullivan 2013a,b), where the same basic procedure is undertaken for investigating modifications to momentum flux due to inertial particles.

2. Numerical details

DNS solves the equations governing conservation of mass, momentum, and energy directly, and solutions

explicitly resolve all length and time scales of a turbulent flow on the computational mesh. Their advantage lies in the fact that the governing equations are solved exactly (within numerical accuracy), thus requiring no modeling, but a disadvantage of DNS lies in the limited range of scales that can be feasibly computed. DNS, therefore, is clearly not a tool for simulating the entire hurricane boundary layer. Instead, we use DNS to gain insight into the physical processes occurring near the high-wind ocean surface in conditions that preclude direct observation or measurement. Such a use of DNS is becoming more prevalent (Abma et al. 2013; Mellado 2010) in the atmospheric sciences for gaining better understanding of small-scale processes.

Numerical details for our work have been described elsewhere (Richter and Sullivan 2013a,b), and only a brief summary is given here. The idealized carrier-phase flow is turbulent Couette flow, which develops between two infinite, parallel plates moving at equal and opposite speeds of $U_0/2$. For studying sensible heat transfer, the bottom plate is given a fixed temperature of $\theta_{\text{bot}} = 300 \text{ K}$, while the top plate is given a temperature of $\theta_{\text{top}} = 295 \text{ K}$. It should be emphasized that throughout this study, the term “heat” refers to passive heat; that is, the temperature is a scalar field and there are no thermal buoyancy forces acting on the carrier phase. This numerical setup, therefore, physically represents a spray-laden, high-wind environment where shear turbulence production dominates buoyancy production. The flow is solved in a horizontally periodic (in x and y) box with height H . The numerical discretization is pseudospectral in the x and y directions, and uses second-order finite differencing in the vertical (z) direction. Time evolution is accomplished using a low-storage, three-stage Runge–Kutta scheme (Spalart et al. 1991).

The equations being solved are the incompressible Navier–Stokes equations (without buoyancy) for mass conservation:

$$\frac{\partial u_j}{\partial x_j} = 0, \quad (1)$$

momentum conservation:

$$\frac{\partial u_i}{\partial t} + u_j \frac{\partial u_i}{\partial x_j} = -\frac{1}{\rho_f} \frac{\partial p}{\partial x_i} + \nu_f \frac{\partial u_i}{\partial x_j \partial x_j} + \frac{1}{\rho_f} F_i, \quad (2)$$

and energy conservation:

$$\frac{\partial \theta}{\partial t} + u_j \frac{\partial \theta}{\partial x_j} = \alpha \frac{\partial^2 \theta}{\partial x_j^2} + \dot{Q}. \quad (3)$$

Here, u_i is the fluid velocity, ρ_f is the fluid density, θ is the fluid temperature, and α is the fluid thermal diffusivity.

The term F_i represents the momentum coupling force between the dispersed phase (particles) and the surrounding fluid, and likewise \dot{Q} represents the energy coupling between the two phases.

For the dispersed phase, individual Lagrangian point particles are tracked, each of which possesses a location, velocity, and temperature determined by the following equations:

$$\frac{dx_i}{dt} = v_i, \quad (4)$$

$$\frac{dv_i}{dt} = (1 + 0.15\text{Re}_p^{0.687}) \frac{1}{\tau_p} (u_{f,i} - v_i), \quad \text{and} \quad (5)$$

$$\frac{d\theta_p}{dt} = -\frac{\text{Nu}}{3\text{Pr}_f} \frac{c_{p,f}}{c_{p,p}} \frac{1}{\tau_p} (\theta_p - \theta_f). \quad (6)$$

In Eqs. (4)–(6), x_i denotes the particle position (which does not necessarily coincide with the carrier-phase computational mesh), v_i denotes the particle velocity, and θ_p denotes the particle temperature. Furthermore, $u_{f,i}$ and θ_f are the carrier-phase velocity and temperature interpolated, using sixth-order Lagrange polynomials, to the particle location. The terms $c_{p,f}$ and $c_{p,p}$ are the specific heats of the fluid and particle, respectively. The quantity τ_p is the acceleration time scale of the particle, given by the Stokes relation $\tau_p = \rho_p d_p^2 / 18\mu_f$, where d_p is the particle diameter and μ_f is the fluid dynamic viscosity.

Since the point-particle approach is being used (as opposed to resolving the flow around each individual particle), momentum and heat transfer at the particle surface is parameterized. In Eq. (5), the term containing Re_p is a Reynolds number correction to the analytic Stokes drag over a sphere, where Re_p is the particle Reynolds number defined as $\text{Re}_p = |u_{f,i} - v_i| d_p \rho_f / \mu_f$ (Clift et al. 1978). In Eq. (6), Nu is the particle Nusselt number, given empirically (Ranz and Marshall 1952) as a function of the particle Reynolds number and fluid Prandtl number ($\text{Pr}_f = \mu_f / \rho_f \alpha$):

$$\text{Nu} \equiv \frac{\bar{h} d_p}{\alpha \rho_f c_{p,f}} = 2 + 0.6 \text{Re}_p^{1/2} \text{Pr}_f^{1/3}, \quad (7)$$

where \bar{h} is the average heat convection coefficient over the particle surface. Since the motivation for this study is sea spray suspended in near-surface air, the ratio of specific heat is set to that of air and water at 300 K: $c_{p,f}/c_{p,p} = 0.24$, and the Prandtl number is set to that of air: $\text{Pr}_f = 0.71$. In a typical simulation, particle Reynolds numbers remain $O(1)$, and therefore typical values of Nu averaged

over the particles remain roughly between 2 (the zero-Reynolds-number case) and 5.

At each time step, after the carrier-phase equations are advanced, Eqs. (4)–(6) are solved for every particle in the domain, updating its position, velocity, and temperature given the local fluid velocity and temperature. The heat and momentum received by an individual particle is projected onto the carrier-phase computational mesh with opposite sign, reflecting a two-way coupling of energy and momentum between phases, and these are represented by the terms F_i and \dot{Q} in Eqs. (2) and (3), respectively.

The point-particle approximation assumes that the particles being represented are much smaller than the smallest turbulent length scales in the flow. For this reason, they can be represented as point sources of heat and momentum. In the high-wind marine boundary layer, however, we estimate using the approximation of Bister and Emanuel (1998) for near-surface dissipation that for 10-m wind speeds near 50 m s^{-1} , the Kolmogorov length is $O(100 \mu\text{m})$. This is computed using Eq. (6) of Bister and Emanuel (1998) with $C_D = 2 \times 10^{-3}$ at a height of 10 m [a similar result is obtained from the dissipation expression of Businger and Businger (2001)]. This value lies near the peak of typical spray size distributions (Andreas 1998; Fairall et al. 2009; Mueller and Veron 2009) [in fact, Andreas et al. (2008) find that droplets with radii near $100 \mu\text{m}$ represent well the total integrated spray heat flux contribution], implying that spray droplets are potentially near or possibly exceed the local Kolmogorov length scales. We expect the momentum coupling to be more sensitive than the thermal coupling to this possible violation of the point-particle approximation. Unfortunately, because of severe computational constraints, we cannot avoid this approximation and do not anticipate changes in our basic conclusions regarding the effect of spray on near-surface fluxes.

In the following sections, numerical experiments are carried out where the dispersed-phase mass loading ϕ_m (defined as the ratio of the total dispersed-phase mass to the total carrier-phase mass in the system), the dispersed-phase Stokes number ($\text{St}_K \equiv \tau_p / \tau_K$, where τ_K is the Kolmogorov time scale at the channel centerline), and the coupling combinations of sensible heat and momentum are varied. The mass loading is an indication of the spray concentration, while the Stokes number gives an indication of the relative inertial resistance of the spray particle to external motions. Unless otherwise noted, all simulations have a bulk Reynolds number of $\text{Re}_b \equiv U_0 H / \nu_f = 8100$, which corresponds to a friction Reynolds number of approximately $\text{Re}_\tau \equiv u_* (H/2) / \nu_f \approx 122$, where $\nu_f = \mu_f / \rho_f$ is the fluid dynamic viscosity and u_* is the friction velocity, defined through the wall stress τ_w as

$u_* \equiv (\tau_w/\rho_f)^{1/2}$. The simulations are initialized with unladen, turbulent velocity and temperature fields, and particles are initially distributed homogeneously throughout the domain. After reaching a statistically steady state, spatial (over the homogeneous x and y directions) and temporal averages are collected over a nondimensional time of $tU_0/H > 6000$.

Finally, before presenting simulation results, a word on how to interpret this study is needed. The choice of turbulent Couette flow is not meant to literally represent the high-wind surface of the ocean. Rather, the simulations presented here are meant to illustrate how fluxes of passive sensible heat can be modified across a region of particle-laden turbulence that has similar characteristics to shear-dominated (i.e., neutrally buoyant), spray-laden flows immediately above the ocean surface. As will be discussed in the following section, Couette flow has the unique property that the total flux of heat is constant with height, and this not only mimics the constant-flux layer of the lower atmospheric boundary layer but allows for systematically making distinctions between cases with varying dispersed-phase characteristics.

Because this study is directed toward a basic, mechanistic understanding of heat fluxes in a turbulent environment in the presence of droplets (as opposed to a direct representation of the air–sea interface), the results and simulation parameters are cast in terms of dimensionless quantities throughout. Nevertheless, it is worthwhile to place the simulations into a physical context. In dimensional units, the plate velocity difference U_0 ranges from 3.18 to 7.07 m s^{-1} , while the domain height ranges between $H = 0.04$ and 0.16 m over the various Reynolds numbers considered. This results in a horizontal domain with sides ranging between approximately 0.25 and 1 m . The droplets have radii of $100 \mu\text{m}$ compared to a centerline Kolmogorov length of approximately $400 \mu\text{m}$. Since this relationship between the droplet radius and Kolmogorov scale was held fixed over all simulations, the particle density must be allowed to vary between 100 and 8000 kg m^{-3} in order to maintain specific particle Stokes numbers. The mass fraction is chosen to be 0.25 (unless otherwise noted), which, rather than attempting to quantitatively match existing droplet concentration measurements, is selected to represent the qualitatively high concentrations that likely exist in the immediate vicinity of the high-wind surface.

One last point should be made regarding the physical processes included here. While the current study incorporates momentum and sensible heat coupling between the phases, it does not consider droplet evaporation, which is essential for fully understanding near-surface thermodynamic exchanges. By neglecting particle evaporation, we are not suggesting that sensible heat exchange

between the particles and carrier phase is somehow more important than latent heat exchange; instead, our goal is to first understand the simpler case of passive sensible heat transfer and add evaporative physics in future studies. The same can be said of salinity and polydispersity effects.

3. Results and discussion

a. Flux profiles

In Richter and Sullivan (2013a) we decompose the total flux of streamwise momentum into contributions from viscous stress, turbulent motions, and particle flux. For Couette flow, it can be shown that the total momentum flux remains constant across the channel height (where z is the distance from bottom wall), which provides an ideal setup for evaluating the relative effects of various sizes and concentrations of particles on cross-channel transport. The same process can be done for the total sensible heat flux $H_{T,\text{total}}$ that is, the total heat flux across the channel can be shown to be constant with height and is decomposed in the following way:

$$\begin{aligned} H_{T,\text{total}} &= \rho_f c_{p,f} \langle w' \theta' \rangle - \rho_f c_{p,f} \alpha \frac{\partial \theta}{\partial z} - \rho_f c_{p,f} \int_0^z \langle \dot{Q}(z^*) \rangle dz^* \\ &\equiv H_{T,\text{turb}} + H_{T,\text{diff}} + H_{T,\text{part}}, \end{aligned} \quad (8)$$

where the first, second, and third terms on the right-hand side of Eq. (8) are the turbulent sensible heat flux, the (molecular) diffusive heat flux, and the heat flux contribution from the dispersed phase.

The heat flux contribution from the dispersed phase can be written in terms of particle statistics after performing an energy balance on the dispersed phase:

$$\int_0^z \langle \dot{Q}(z^*) \rangle dz^* = -\frac{c_{p,p}}{c_{p,f}} \frac{\langle c \rangle}{\rho_f} \langle w'_p \theta'_p \rangle_c, \quad (9)$$

where $c(z)$ is the dispersed-phase mass concentration, w'_p is the particle fluctuating wall-normal velocity, and θ'_p is the fluctuating particle temperature. The notation $\langle \cdot \rangle_c$ indicates averaging over the dispersed phase. Equation (9) indicates that the heat transported by the particles is related to the mass-weighted turbulent flux of the dispersed phase. Physically, this represents the heat that the particles carry as they are transported by carrier-phase wall-normal velocity fluctuations.

In a series of runs, the mass fraction was held constant at $\phi_m = 0.25$ and the particle inertia was varied between $\text{St}_K \approx 1$ and $\text{St}_K \approx 10$. For each Stokes number, all combinations of dynamical couplings are considered: momentum coupling (on, off) and thermal coupling (on, off).

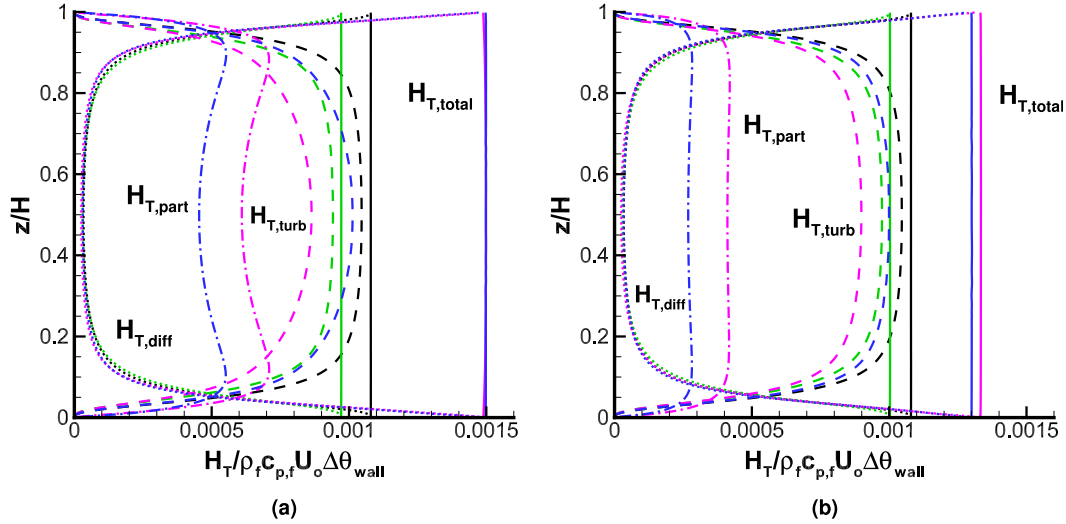


FIG. 1. Heat flux components $H_{T,diff}$ (dotted), $H_{T,part}$ (dashed-dotted), $H_{T,turb}$ (dashed), and $H_{T,total}$ (solid) for (a) $St_K \approx 1$ and (b) $St_K \approx 10$. Colors indicate couplings: black is unladen (both uncoupled), magenta is both thermal and momentum coupling on, green is momentum coupling on and thermal coupling off, and blue is momentum coupling off and thermal coupling on.

The heat flux components for these cases are shown in Fig. 1.

In Figs. 1a and 1b, the trend is generally the same for particles of $St_K \approx 1$ and $St_K \approx 10$ as the couplings are modified. Starting with the unladen (black) case, the effect of momentum coupling only (green) is to reduce the total sensible heat flux across the channel—hence the slight leftward shift of the total flux component. In this case the particles are not contributing to the transport of sensible heat, and since the diffusive flux does not substantially change for any of the cases (except at the walls), the reduction in total flux is entirely due to a reduction in turbulent flux for both particle types. As shown in Richter and Sullivan (2013a), momentum coupling between the carrier and dispersed phases leads to a dampening of wall-normal velocity fluctuations, and this is manifested in the current case as less effective wall-normal turbulent transport of passive heat. For both particle masses (St_K), the reduction of the total heat flux is similar in magnitude.

Starting again with the unladen case (black), the effect of adding thermal coupling only (blue) is to significantly increase the total heat flux across the channel. Here, the additional particle heat transport is large—the dispersed-phase heat flux is about 45% of $\langle w'\theta' \rangle$ (30% of the total) for the $St_K \approx 1$ particles and 27% of $\langle w'\theta' \rangle$ (20% of the total) for the more massive particles. Since the particles have a heat capacity roughly 4 times larger than that of the surrounding air, they are able to efficiently transport a large amount of heat as they travel from the bottom (hot) to the top (cold) wall. With this additional source

of heat transport, the mean temperature gradient is decreased across most of the channel (except very close to the walls—see the diffusive flux) as heat is more effectively mixed. This leads to a slight reduction in the turbulent flux.

When momentum coupling is turned on in addition to thermal coupling (magenta), a further reduction in the turbulent flux is observed owing to the damping of wall-normal fluctuations [as was the case for momentum coupling only (green), as stated above]. In this case, however, the reduced ability of carrier-phase turbulence to carry heat from the bottom to the top wall is compensated by an increase in the heat carried by the dispersed phase. For both Stokes numbers, the total flux remains nearly constant. This is qualitatively similar to our previous studies (Richter and Sullivan 2013a,b) where reductions in carrier-phase momentum flux were almost exactly compensated by momentum flux of the particles. With both couplings turned on, a hot parcel of air traveling away from the bottom wall transfers its upward momentum and heat to an element of the dispersed phase, netting zero additional total heat transfer since the dispersed phase is merely transferring heat that would have otherwise been delivered by the carrier phase. Ultimately, for both couplings turned on, the heat being carried by the dispersed phase is roughly 40% of the total flux for the $St_K \approx 1$ particles and 30% of the total flux for the $St_K \approx 10$ particles.

Finally, a discussion should be made regarding the effect of particle mass. Figure 1a shows that particles with $St_K = O(1)$ are more effective at transporting heat

than those with $St_K = O(10)$ (Fig. 1b), which is consistent with our previous findings for momentum flux (Richter and Sullivan 2013a). As argued in Richter and Sullivan (2013a), preferential concentration, which occurs when particles are centrifuged from regions of high vorticity leading to locally high concentrations, is responsible for the enhanced transfer. At a Stokes number of zero, particles act as fluid tracers and would therefore carry no net heat or momentum. At sufficiently high Stokes number, particles are too massive to experience a large change in their trajectory and thus their concentration stays relatively homogeneous throughout the domain. Between these extremes, peaking at $St_K = O(1)$ (Rouson and Eaton 2001), the particle acceleration time scale is close in magnitude to the time scale of the smallest turbulent motions, resulting in clusters of particles that effectively transport heat and momentum away from the wall as they are ejected by near-wall vortical motions.

Figure 2 illustrates this phenomenon for the two Stokes numbers currently being studied. One feature of turbulent Couette flow is the presence of large streamwise rollers that exist in the channel center plane, whose imprint can be seen in the large low-speed streaks near the wall (blue streaks in Figs. 2a and 2c). These are in addition to smaller-scale streaks typical of wall-bounded turbulent flows. Low-speed streaks are typically correlated with regions of relatively warm fluid (Figs. 2b and 2d), since these locations indicate the upwelling of slow, warm fluid from the wall in convergence zones between near-wall vortices (Adrian 2007). In the same way, these regions are also capable of transporting large numbers of particles away from the wall (Figs. 2b and 2d), but this process depends on the mass of the particle. $St_K = O(1)$ particles are much more easily influenced by the surrounding flow than the $St_K = O(10)$ particles; therefore, they preferentially concentrate into these same upwelling regions as they are centrifuged out of near-wall vortical motions. The $St_K = O(10)$ particles, on the other hand, cannot adjust to the surrounding fluid as quickly, and only accumulate in the strongest regions of upwelling, remaining much more uniformly distributed on average. In this way, the $St_K = O(1)$ particles are more effective at transporting heat away from the walls (seen in Fig. 1) since their location is more highly correlated with wall-normal motions, allowing them to carry heat gained from the warm, near-wall fluid.

b. Transfer coefficients

The fluxes displayed in Fig. 1 can be cast in terms of a model transfer coefficient C_H . For the Couette geometry, we define C_H using the computed values of the heat flux at the channel centerline:

$$H_T(H/2) = \rho_f c_{p,f} C_H U_0 \Delta\theta_{\text{wall}}. \quad (10)$$

Here, U_0 is used as the velocity scale, and $\Delta\theta_{\text{wall}}$, the temperature difference between the top and bottom plate, is used as the temperature scale.

As noted in Richter and Sullivan (2013b), a choice exists between using $H_{T,\text{total}}$ or only $H_{T,\text{turb}}$ in defining the heat transfer coefficient:

$$C_{H,\text{total}} = \frac{H_{T,\text{total}}(H/2)}{\rho_f c_{p,f} U_0 \Delta\theta_{\text{wall}}} \quad \text{and} \quad (11)$$

$$C_{H,\text{turb}} = \frac{H_{T,\text{turb}}(H/2)}{\rho_f c_{p,f} U_0 \Delta\theta_{\text{wall}}}. \quad (12)$$

The difference between these quantities is the heat flux contributed by the dispersed phase (and a small contribution from the diffusive flux), and $C_{H,\text{turb}}$ is based on the turbulent flux that in practice would result from solely measuring the eddy correlation $\langle w'\theta' \rangle$.

In an additional series of runs, the mass fraction is varied between $\phi_m = [0.1, 0.25, 0.5]$ for both particle Stokes numbers. The two different measures of C_H are plotted in Fig. 3 as a function of ϕ_m (ϕ_m can be thought of as a surrogate for wind speed since spray concentrations increase with wind).

Figure 3 illustrates that with increasing concentrations of dispersed phase, the total heat flux (squares) increases nearly linearly. The contribution from the turbulent flux (circles), however, decreases with increasing concentration, as more and more heat is being carried by the particles. For any given mass fraction, this trend is enhanced when $St_K = O(1)$ (blue symbols).

As the mass loading ϕ_m increases, the total available particle mass that can contribute to wall-normal transport of heat increases. This simple fact is the primary reason behind the increase of C_H in Fig. 3. As we mention in the previous section, the ratio of the specific heat of water versus that of air is roughly a factor of 4, so an individual particle is much more efficient at transporting heat than the same mass of air. At the same time, the time scale governing the thermal response of the particle is roughly 5 times larger than that for air for the particles chosen for this study [this can be computed from the terms in the right-hand sides of Eqs. (5) and (6) using $Re_p \approx 1$ and $Nu \approx 2$], which physically implies that the particle takes 5 times longer to adjust its temperature than its velocity when entering a region of differing fluid velocity and temperature. Therefore, an individual particle often finds itself in temperature disequilibrium as it is transported by carrier-phase motions, and this further contributes to its effective transport of heat.

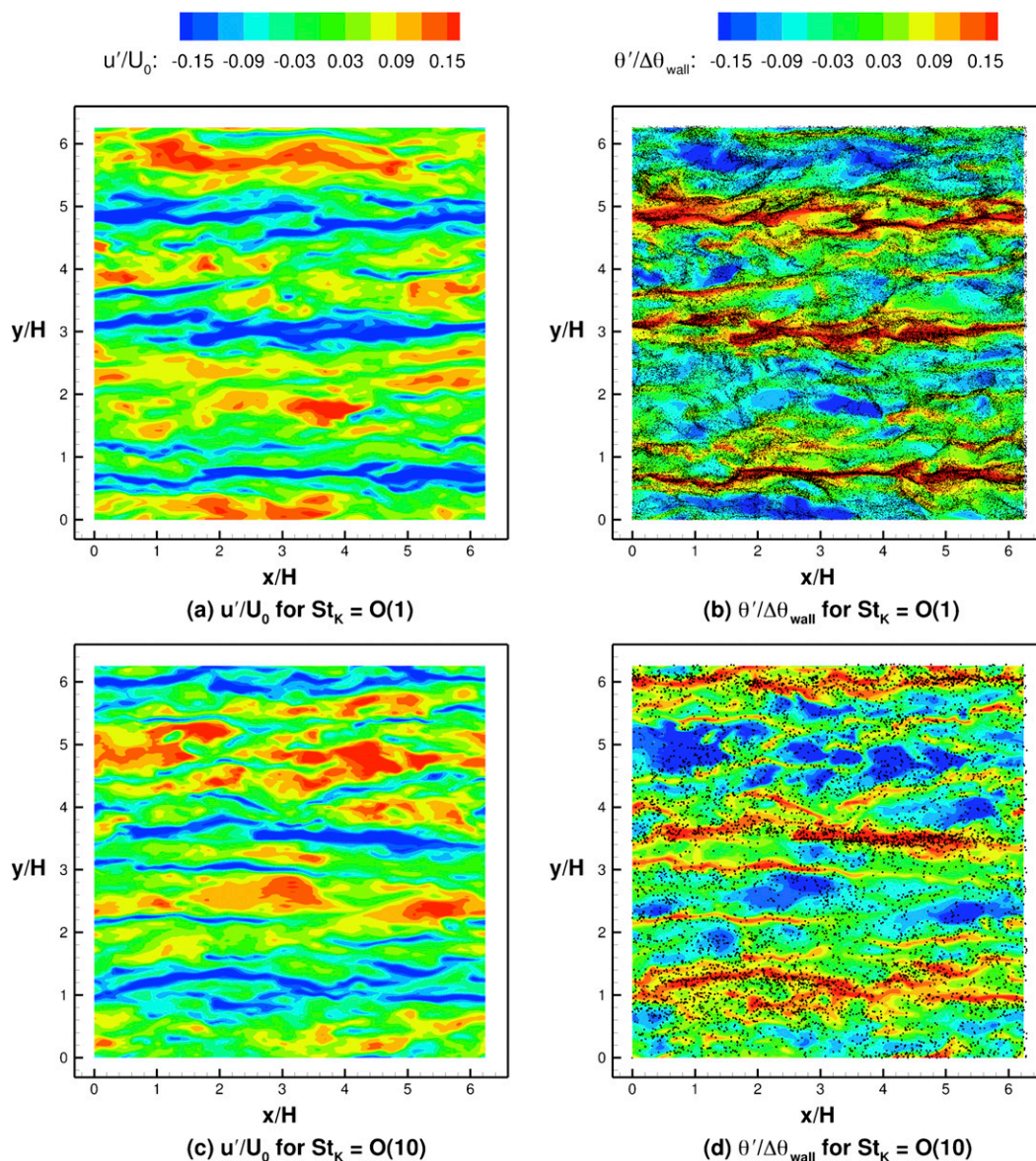


FIG. 2. Contours of streamwise velocity fluctuations (a),(c) normalized by U_0 and contours of temperature fluctuations and (b),(d) normalized by $\Delta\theta_{wall}$ (the temperature difference between the bottom and top walls of the domain) at a height of $z/H = 0.1$. Instantaneous particle locations are included in (b),(d). (top) Contours for $St_K = O(1)$ and (bottom) contours for $St_K = O(10)$. Both cases have momentum and thermal coupling active. Note particle sizes are not to scale.

The bulk flux algorithm of Andreas et al. (2008) for computing sensible and latent heat fluxes is based on the idea that so-called interfacial fluxes scale differently than spray fluxes with wind speed, and efforts are made by the authors to separate these behaviors using an existing interfacial flux model (COARE 2.6; Fairall et al. 1996) and the HEXOS (DeCosmo et al. 1996) and Fronts and Atlantic Storm-Track Experiment (FASTEX; Joly et al. 1997) datasets. While the current simulations take place in an idealized geometry and are not meant to

exactly represent the high-wind marine boundary layer, the qualitative importance of spray in exchanging sensible heat agrees with the findings of Andreas et al. (2008). Namely, at high wind speeds where spray concentrations are large, the sensible heat transfer is mostly due to spray-mediated exchanges. At the highest mass fraction simulated ($\phi_m = 0.5$), the flux of heat due to spray exceeds that of the turbulent carrier phase—an occurrence that the flux algorithm of Andreas et al. (2008) predicts around 10-m wind speeds of roughly 27 m s^{-1} (see their Fig. 8).

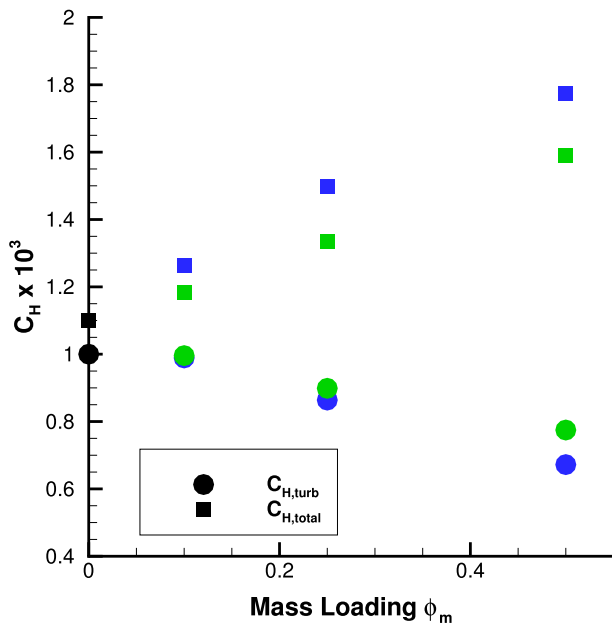


FIG. 3. Values of $C_{H,total}$ and $C_{H,turb}$ [defined in Eqs. (11) and (12)] as a function of ϕ_m . Black symbols indicate the unladen case. Green symbols are for $St_K \approx 10$ and blue symbols are for $St_K \approx 1$. Squares and circles are denoted in the legend.

The increase of total sensible heat with spray concentration does not appear to be confirmed in measurements, however. The HEXOS dataset (DeCosmo et al. 1996) measures sensible heat exchange and, according to Andreas et al. (2008), captures the effects of spray despite no observable increase in C_H with wind speed. More recent measurements of total enthalpy fluxes (Bell et al. 2012; Jeong et al. 2012; Zhang et al. 2008) also do not indicate an observable increase of the enthalpy exchange coefficient with wind speed. While these appear to be in contradiction with our simulations, a few important items must be noted. First, the total enthalpy flux is not the same as sensible heat flux, and the effects of evaporation and latent heat fluxes are not yet included in our simulations. Second, these measurements do not distinguish between interfacial (carrier phase) fluxes and spray-mediated fluxes. Andreas (2011) argues, for the case of the HEXOS data, that the lack of wind speed dependence on total exchange coefficients is due to a simultaneous reduction of the interfacial transfer coefficients with a similar-in-magnitude increase of the coefficient due to spray-mediated transfer. That is, a constant heat transfer coefficient does not necessarily imply an absence of spray effects. Finally, observational uncertainty could also explain the lack of wind speed dependence on C_K found in the existing observational studies. Since measurements of C_K (and C_H) are extremely difficult to make in high-wind conditions,

these studies must be interpreted with the understanding that they have significant limitations. For example, many of the CBLAST measurements were taken at heights near the boundary layer height (Black et al. 2007), well above the surface layer, and the experiments done by Jeong et al. (2012) were done in a finite-length tunnel, which leads to uncertainty in the amount of re-entrant spray present in the experiment (and thus their estimate of total heat flux from the surface).

It is also interesting to consider the ratio C_H/C_D in the current simulations as an indicator of the ratio C_K/C_D , which has been identified as an important parameter in predicting maximum possible tropical cyclone strength (Emanuel 1995). As mentioned above, the sensible heat flux is a fundamentally different quantity than the enthalpy flux, and the present numerical setup is not meant to provide quantitative information about the marine boundary layer. However, information about the relative importance of spray can be identified.

Figure 4 shows C_H/C_D as a function of ϕ_m with the same symbol notation as in Fig. 3. As in Richter and Sullivan (2013b), the model drag coefficient for the Couette flow simulations can also be defined based solely on the turbulent stress ($C_{D,turb}$) or the total ($C_{D,total}$), which includes momentum carried by the dispersed phase. Although it is not shown here, a monotonic reduction of the turbulent momentum flux coefficient $C_{D,turb}$ occurs with increasing ϕ_m , while the total increases only slightly. Therefore, the quantity $C_{H,total}/C_{D,total}$ (squares) is mostly dictated by the behavior of $C_{H,total}$, which increases nearly linearly with ϕ_m for both particle Stokes numbers. Because $C_{D,turb}$ decreases with increasing ϕ_m , the quantity $C_{H,turb}/C_{D,turb}$ (circles) decreases less rapidly with ϕ_m than does $C_{H,total}$ alone. Figures 3 and 4 illustrate an important point: if the transfer of heat and momentum carried by the dispersed phase is ignored (e.g., by only measuring the turbulent fluxes in the presence of spray), the measured behavior of the sensible heat exchange coefficient and its strength relative to the momentum exchange coefficient can significantly underestimate the total.

c. Injection

The simulations described up to this point have not considered a gravitational force on the particles, and since the particles collide elastically with the walls, none enter or exit the domain. To create a situation more akin to the physical air–sea interface, additional simulations are performed where gravity acts to settle the particles downward (buoyancy is still neglected in the carrier-phase motions). For every particle that leaves the domain, a new particle is injected upward from the bottom wall at a random location with a velocity chosen

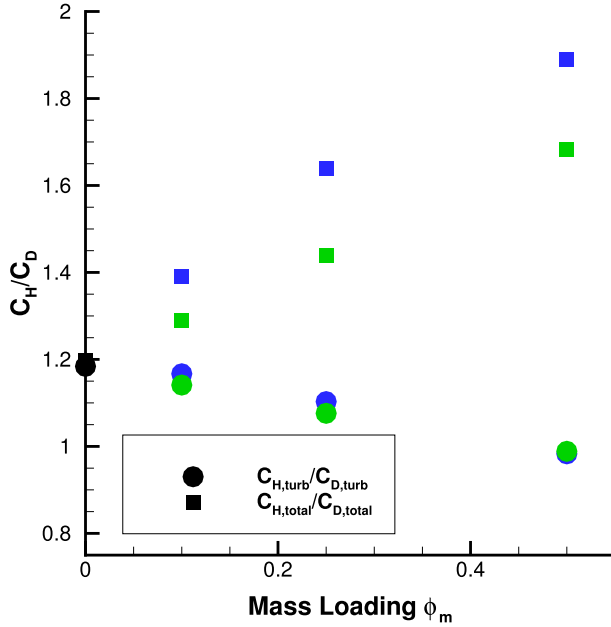


FIG. 4. Values of $C_{H,\text{total}}/C_{D,\text{total}}$ and $C_{H,\text{turb}}/C_{D,\text{turb}}$ as a function of ϕ_m . Black symbols indicate the unladen case. Green symbols are for $St_K \approx 10$ and blue symbols are for $St_K \approx 1.3$. Squares and circles are denoted in the legend.

from a uniform random distribution between 0 and $U_0/2$ and a temperature of $\theta_{\text{inj}} = 300$ K. That is, each particle enters the domain with the same temperature as the bottom wall in an attempt to mimic spray originating from the ocean surface. Two runs are made, each with a mass fraction of $\phi_m = 0.25$: one for $St_K = 13.5$ and one for $St_K = 1.3$. The gravitational acceleration is modified in each case to set $v_g/v_K = 0.4$, where v_g is the particle

settling velocity and v_K is the Kolmogorov velocity scale at the channel centerline. Thus, the strength of the turbulence relative to the particle-settling tendency is equal in both cases, despite the difference in particle inertia.

Figure 5 shows the mean number concentration and mean temperature profiles for the injection cases. In the presence of gravity, the more massive particles (red) distribute nearly homogeneously across the channel height, while the less massive particles (green) show a decrease in their concentration with height since their initial injection velocity (which is in the same range for both particle Stokes numbers) is not adequate to propel them beyond the channel midplane before they are swept up by carrier-phase motions. Note that the vertical distributions of particles is not what one would expect in the physical system since this is an idealized scenario where the gravitational settling has been set to match turbulent fluctuations. Figure 5b shows that the injection of particles substantially increases the carrier-phase temperature across the channel, indicating that the dispersed phase is injecting large amounts of heat into the system.

To illustrate this heat injection more directly, Fig. 6 shows the same flux profiles as shown in Fig. 1. Comparing the total fluxes with those from the previous simulations (Fig. 1), it is clear that the injection of particles increases the total amount of heat being transported from the bottom to the top boundary, which is expected since external heat is now being added to the domain. Focusing only on the $St_K = 1.3$ (green) case, the particle heat flux greatly exceeds the turbulent flux in the lower half of the channel, while a sharp dropoff in particle flux coinciding with the decrease in particle

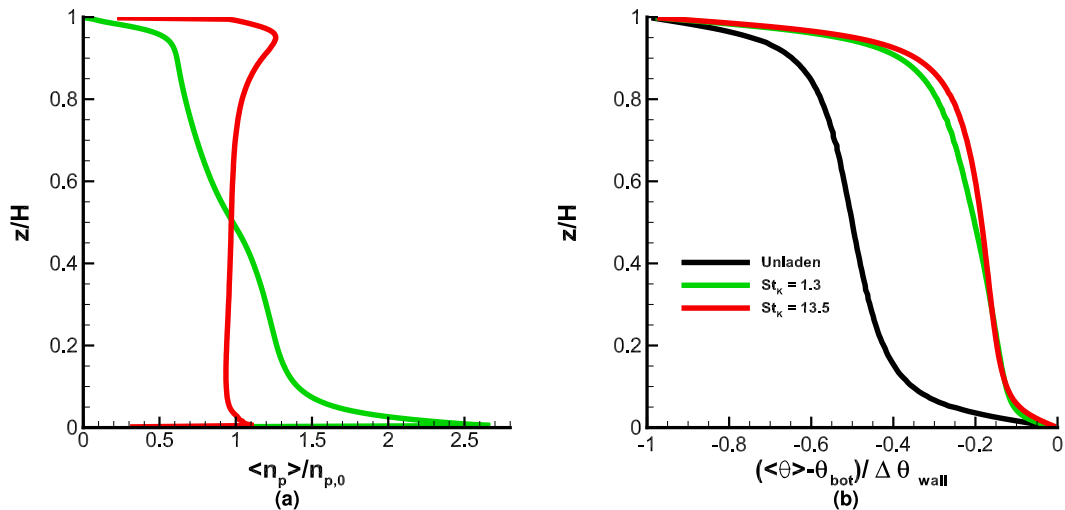


FIG. 5. (a) Mean number concentration $\langle n_p \rangle$ normalized by the homogeneous concentration $n_{p,0}$, as a function of channel height. (b) Mean temperature deficit $\langle \theta \rangle - \theta_{\text{bot}}$ normalized by $\Delta \theta_{\text{wall}}$. Black curves are for unladen case, green curves are for $St_K = 1.3$ case, and red curves are for $St_K = 13.5$ case.

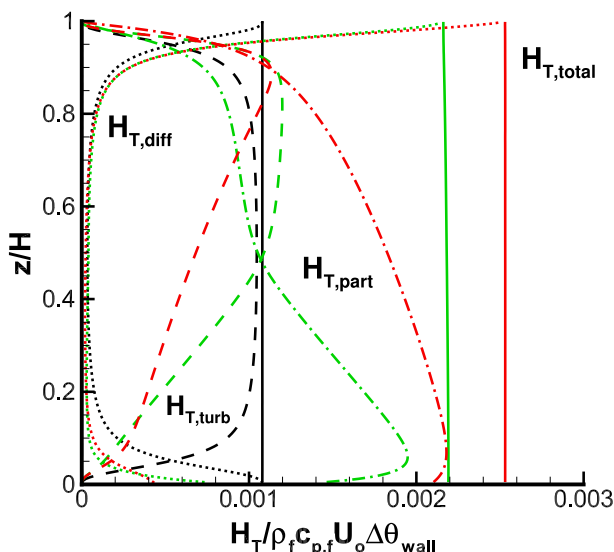


FIG. 6. Flux components for the injection cases. Black curves are for the unladen case, green for $St_K = 1.3$, and red for $St_K = 13.5$. Solid lines indicate $H_{T,\text{total}}$, dashed-dotted lines are for $H_{T,\text{part}}$, dashed lines are for $H_{T,\text{turb}}$, and dotted lines are for $H_{T,\text{diff}}$.

concentration causes the turbulent flux to exceed the particle flux in the upper half of the domain. For the higher Stokes number (red), the dispersed-phase heat flux is generally larger in magnitude (as is the total heat flux), which is mostly due to the larger amount of heat contained in each individual particle entering the system.

For Couette flow, the total flux must remain constant with height, so the decrease in dispersed-phase heat flux seen in the $St_K = 1.3$ case near the channel centerline is compensated by an increase in turbulent flux in the upper half of the domain. The extra heat flux due to the injection of the dispersed phase is thus eventually carried by turbulent motions in regions where the particle concentration becomes low. If one interprets this in the context of the spray-containing layer in the high-wind marine atmospheric surface layer, then it would indicate that any enhanced heat flux from the surface due to the ejection of spray would be present in direct (i.e., eddy correlation) turbulent flux measurements taken above the spray layer, assuming that the total flux was constant with height (as is normally assumed for the surface layer).

In the CBLAST field campaign (Black et al. 2007), this is done for moisture fluxes (Drennan et al. 2007) using aircraft measurements taken at various heights throughout the atmospheric boundary layer (but well above the surface layer), and enhanced moisture fluxes are not found at high winds. Therefore, if spray is in fact enhancing fluxes of sensible heat (in our case) or moisture (in their case), then some competing mechanism

may exist that offsets this enhancement, such as a compensating reduction in interfacial fluxes (such that the total remains the same), or through thermodynamic processes occurring near the surface that are not accounted for in either the current simulations or other spray modeling attempts.

d. Effect of Reynolds number

Finally, the effect of the Reynolds number of the flow is investigated in order to establish an idea of whether the changes to heat flux described in the previous sections would be expected at more realistic Reynolds numbers. As the Reynolds number increases, the separation between the largest, energy-containing scales and the dissipation scales grows. Since the particle diameters are on the order of the dissipation scales or smaller, the question of whether they can remain effective when turbulent heat transport is being accomplished by motions much larger than their size is essential. To therefore probe the effectiveness of the particle contribution to heat fluxes at larger-scale separations, identical simulations to those originally described (i.e., no particle injection or particle gravity) are run with both thermal and momentum coupling turned on, $\phi_m = 0.25$, and for both $St_K = O(1)$ and $St_K = O(10)$. The original case has $Re_\tau \approx 125$, and two additional simulations of $Re_\tau \approx 320$ and $Re_\tau \approx 900$ are added. In these cases, the Reynolds number is increased by successively doubling H as well as increasing U_0 . The bulk Reynolds number varies as $Re_b = [8100, 24\,000, 72\,000]$. The grid resolution is increased in order to maintain the same grid spacing as a ratio of the Kolmogorov turbulence length scale.

Figure 7 shows the contributions from the various flux components, just as in Fig. 1, for each Reynolds number. Several features are observed as the Reynolds number is varied. First, the influence of thermal diffusion (dotted lines) is further confined to regions near the walls as Re_b increases, as is expected at higher Reynolds numbers. Second, focusing only on the unladen cases (black curves), the total heat flux, when normalized by $U_0 \Delta \theta_{\text{wall}}$, decreases with Reynolds number. In dimensional terms (not shown), the total flux increases with Re_b , but not as quickly as U_0 . Therefore, the normalization causes a downward shift in the normalized heat flux.

When the effect of particles is introduced, the total heat fluxes for all cases increase substantially—more so for the $St_K = O(1)$ cases (blue curves) than for the $St_K = O(10)$ cases (green curves). For $St_K = O(1)$, the increase in the total flux is above 40% for all Reynolds numbers, and is due entirely to a large increase in the particle heat flux. For each St_K , the normalized value of $H_{T,\text{part}}$ is nearly unchanged as Re_b is increased, suggesting that the particle flux scales strongly with the temperature

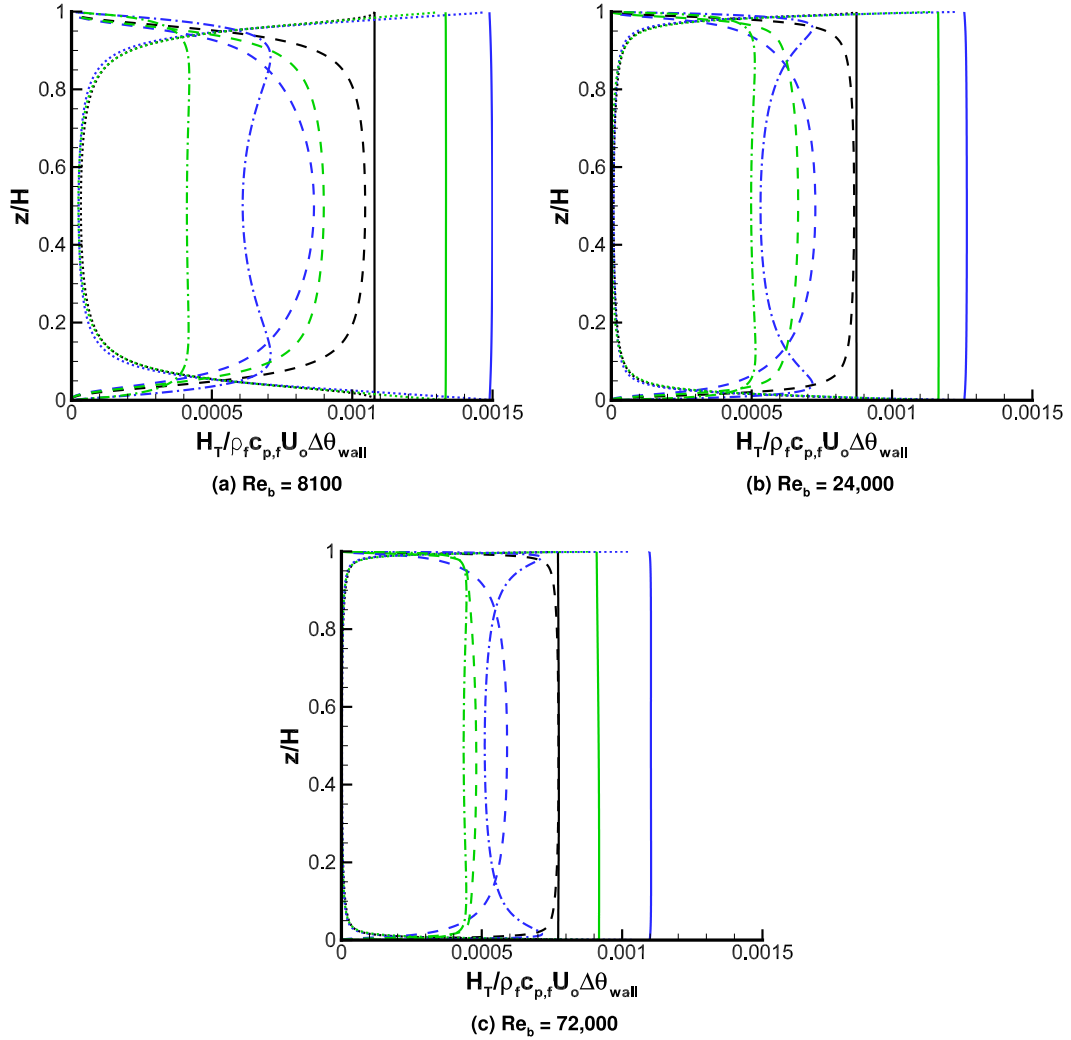


FIG. 7. Heat flux components $H_{T,diff}$ (dotted), $H_{T,part}$ (dashed-dotted), $H_{T,turb}$ (dashed), and $H_{T,total}$ (solid) for (a) $Re_b = 8100$, (b) $Re_b = 24000$, and (c) $Re_b = 72000$. Colors indicate St_K : black is unladen (both uncoupled), blue is $St_K = O(1)$, and green is $St_K = O(10)$.

difference between the walls, which is consistent with the physical picture that particles absorb heat near the bottom surface and later release it near the top.

The nearly constant values of particle heat flux emphasize the dramatic changes to the turbulent heat flux. The unladen turbulent heat flux decreases with Reynolds number when normalized by $U_0 \Delta \theta_{wall}$, again owing to the increase in U_0 . As a fraction of the unladen turbulent heat flux, however, $H_{T,turb}$ for the particle-laden cases decreases with Reynolds number, indicating a change in the turbulent heat transport efficiency. Since for these simulations the momentum coupling between the two phases is active, this reduction in $H_{T,turb}$ is largely due to a decrease in the wall-normal velocity fluctuations (not shown). For $Re_b = 72000$, the particle

and turbulent heat fluxes are nearly equal in magnitude across the channel.

As before, one can define C_H based on the various flux components. In this case, the transfer coefficient $C_{H,part}$ based on the particle flux is included as well. Analogous to Eqs. (11) and (12), we define this quantity as

$$C_{H,part} = \frac{H_{T,part}(H/2)}{\rho_f c_{p,f} U_0 \Delta \theta_{wall}}. \quad (13)$$

Figure 8 shows the C_H quantities as a function of Reynolds number for each value of St_K . The trends described previously can be seen in Fig. 8. Namely, the reduction of both the total and turbulent fluxes for all cases appears linear (on a semilogarithmic plot) with increasing

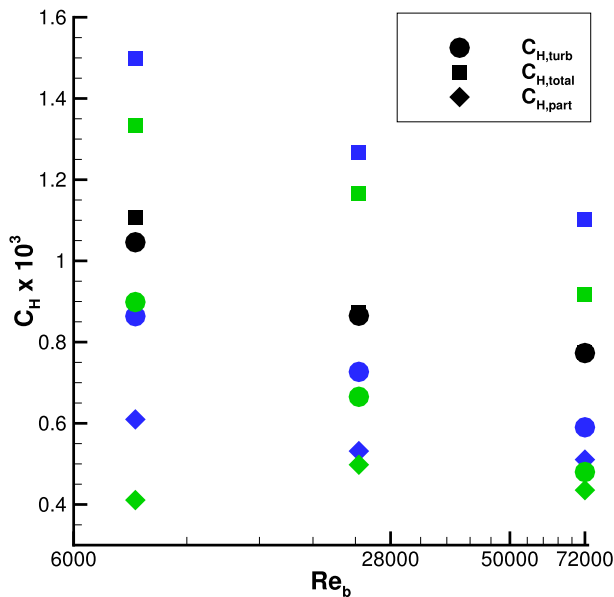


FIG. 8. Values of $C_{H,\text{total}}$, $C_{H,\text{turb}}$, and $C_{H,\text{part}}$ [defined in Eqs. (11)–(13), respectively] as a function of Re_b on a log scale. Black symbols indicate the unladen cases, green symbols are for $St_K \approx 10$, and blue symbols are for $St_K \approx 1$. Symbols are denoted in the legend. Note that for the unladen cases at high Re_b , the black squares lie behind the black circles.

Re_b . Furthermore, for all St_K , the value of $C_{H,\text{total}}$ is substantially larger than its unladen value, while $C_{H,\text{turb}}$ would suggest a significant underestimate of the total heat being carried across the channel. More importantly, Fig. 8 illustrates that the particles, rather than having a diminishing effect as the separation between the smallest and largest scales is enlarged, account for more and more of the total heat flux across the channel. As Re_b is increased, the value of $C_{H,\text{part}}$ remains roughly uniform (as discussed above), while the total value decreases owing to the reduction of $C_{H,\text{turb}}$. Aside from modifying the turbulence, which we will not discuss presently, the particles provide an efficient source of transporting heat between the Couette cell walls, even with increasing scale separation. Although the particle size is small compared to the turbulence length scales, they are transported along motions of all scales, transporting heat with them.

Finally, Fig. 9 plots the ratio C_H/C_D as a function of Reynolds number, using both the turbulent flux values (circles) and total flux values (squares). With increasing Reynolds number, both definitions of C_H/C_D for the unladen cases (black) remain nearly constant. Since Fig. 8 shows that both $C_{H,\text{turb}}$ and $C_{H,\text{total}}$ decrease with Reynolds number for the unladen case, the independence of both definitions of C_H/C_D with Re_b indicates that the turbulent transport of both momentum and heat are changing in the same way as the Reynolds number is

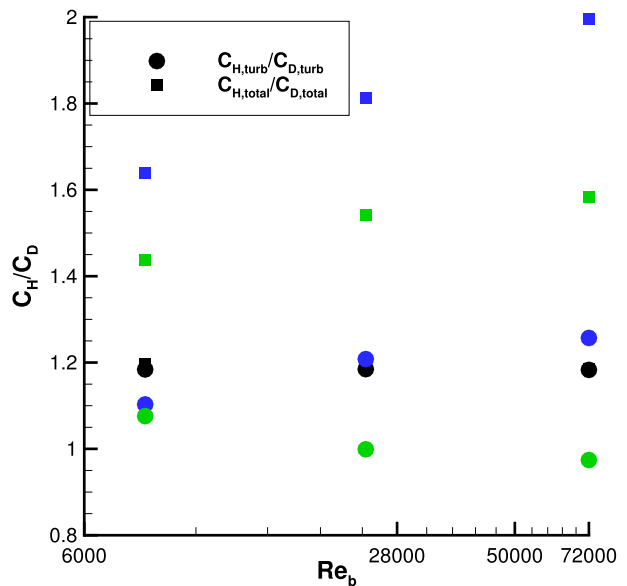


FIG. 9. Values of $C_{H,\text{total}}/C_{D,\text{total}}$ and $C_{H,\text{turb}}/C_{D,\text{turb}}$ as a function of Re_b on a log scale. Black symbols indicate the unladen cases, green symbols are for $St_K \approx 10$, and blue symbols are for $St_K \approx 1$. Symbols are denoted in the legend. Note that for the unladen cases at high Re_b , the black squares lie behind the black circles.

increased. With the effect of particles of either St_K , however, the ratio $C_{H,\text{total}}/C_{D,\text{total}}$ increases substantially with Re_b , illustrating that $C_{D,\text{total}}$ (not shown) decreases with Re_b at a faster rate than $C_{H,\text{total}}$.

At the same time, the dependence of $C_{H,\text{turb}}/C_{D,\text{turb}}$ on Re_b is weaker than that of $C_{H,\text{total}}/C_{D,\text{total}}$, and depends on particle characteristics. Particles with $St_K = O(1)$ have $C_{H,\text{turb}}$ decreasing more slowly relative to $C_{D,\text{turb}}$, while particles with $St_K = O(10)$ show a faster decrease of $C_{H,\text{turb}}$ relative to $C_{D,\text{turb}}$ as Re_b increases. This behavior highlights the difference between the modification of momentum flux (which, again, will not be discussed in detail presently) and the modification of heat flux by the particles. In terms of sensible heat, the particles have the ability to greatly increase the total flux beyond its unladen value by providing a particle flux that can, at high Re_b , be of the same order as the turbulent flux (cf. Fig. 7). The same is generally not true of the momentum flux, where the particles do not cause increases in the total flux beyond the unladen values (not shown).

In this way, while $C_{H,\text{total}}$ still decreases with Re_b in the particle-laden simulations, the rate of decrease is diminished by the additional particle flux (which, recalling from Fig. 8, remains relatively unchanged with Re_b), while $C_{D,\text{total}}$ does not have an analogous mechanism. The result is an increase of the ratio $C_{H,\text{total}}/C_{D,\text{total}}$ with Re_b . This effect is more pronounced when

$St_K = O(1)$. As before, a ratio C_H/C_D computed with turbulent fluxes in regions of high spray concentration would greatly underestimate the same ratio computed with the total fluxes, and this is entirely a result of the enhanced sensible heat flux due to particles.

In the context of the spray-laden marine boundary layer, Figs. 8 and 9 suggest that spray-mediated heat transfer from the water surface will be significant even at atmospheric scales. Figure 8 shows that the particle heat flux is minimally dependent on Re_b . Instead, this spray-mediated transfer scales with the plate temperature difference $\Delta\theta_{\text{wall}}$, indicating a much stronger dependence of the particle heat flux on air–sea temperature differences than characteristics of the near-surface air turbulence. While the current simulations do not claim to simulate the ocean surface, the increase of the particle heat flux as a fraction of the turbulent heat flux is qualitatively similar to the faster scaling of spray-mediated heat flux with wind speed compared to that of the interfacial flux (Andreas et al. 2008).

4. Conclusions

Thermal coupling between a dispersed and carrier phase in turbulent Couette flow is used to examine the ability of spray in the near-surface marine boundary layer to transfer sensible heat to the atmosphere. The direct numerical simulations performed are not an explicit representation of the air–sea interface; rather, the idealized numerical study performed here is used to gain an understanding of the fundamental importance of spray-mediated sensible heat fluxes in a shear-dominated (neutrally buoyant) environment. By monitoring the contributions of the total heat flux from both the turbulent motions of the carrier phase and the dispersed phase, it is found that the dispersed phase greatly enhances the total sensible heat flux across the Couette cell beyond what is done by carrier-phase turbulent motions alone. A single particle, when pushed to the bottom (hot) wall, absorbs heat, which it then carries across the channel as it is transported by turbulent motions. Particles with acceleration time scales of the same order as the near-wall motions [designated by $St_K = O(1)$ here] are more efficient at cross-channel transport since they preferentially concentrate in turbulent ejection regions near the bottom wall. To further demonstrate that spray in the high-wind boundary layer will have this effect, cases were also run with particle injection at the bottom surface, showing an even further enhanced flux of heat across the channel as well as a significant change in the temperature distribution.

The current simulations suggest that spray greatly enhances the flux of sensible heat at the ocean surface,

but this is not seen in many of the available measurements of surface heat, moisture, and enthalpy fluxes. We believe this difference is a combination of the inability of measurements to distinguish between spray-mediated and interfacial fluxes, inherent uncertainty in existing observations, and a lack of evaporative thermodynamics in our simulations.

Acknowledgments. The authors thank Ed Andreas as well as two anonymous reviewers for comments that have greatly improved the quality of the manuscript. The authors would also like to thank the National Science Foundation, which sponsors the National Center for Atmospheric Research, and the Advanced Study Program for financial support. Several of the simulations presented were performed under the Accelerated Scientific Discovery program at NCAR, which we are grateful for.

REFERENCES

- Abma, D., T. Heus, and J. P. Mellado, 2013: Direct numerical simulation of evaporative cooling at the lateral boundary of shallow cumulus clouds. *J. Atmos. Sci.*, **70**, 2088–2102.
- Adrian, R. J., 2007: Hairpin vortex organization in wall turbulence. *Phys. Fluids*, **19**, 041301, doi:10.1063/1.2717527.
- Andreas, E. L., 1998: A new sea spray generation function for wind speeds up to 32 m s^{-1} . *J. Phys. Oceanogr.*, **28**, 2175–2184.
- , 2004: Spray stress revisited. *J. Phys. Oceanogr.*, **34**, 1429–1440.
- , 2010: Spray-mediated enthalpy flux to the atmosphere and salt flux to the ocean in high winds. *J. Phys. Oceanogr.*, **40**, 608–619.
- , 2011: Fallacies of the enthalpy transfer coefficient over the ocean in high winds. *J. Atmos. Sci.*, **68**, 1435–1445.
- , and K. Emanuel, 2001: Effects of sea spray on tropical cyclone intensity. *J. Atmos. Sci.*, **58**, 3741–3751.
- , and J. DeCosmo, 2002: The signature of sea spray in the HEXOS turbulent heat flux data. *Bound.-Layer Meteor.*, **103**, 303–333.
- , P. O. G. Persson, and J. E. Hare, 2008: A bulk turbulent air–sea flux algorithm for high-wind, spray conditions. *J. Phys. Oceanogr.*, **38**, 1581–1596.
- Bao, J.-W., C. W. Fairall, S. A. Michelson, and L. Bianco, 2011: Parameterizations of sea-spray impact on the air–sea momentum and heat fluxes. *Mon. Wea. Rev.*, **139**, 3781–3797.
- Bell, M., M. Montgomery, and K. Emanuel, 2012: Air–sea enthalpy and momentum exchange at major hurricane wind speeds observed during CBLAST. *J. Atmos. Sci.*, **69**, 3197–3222.
- Bianco, L., J.-W. Bao, C. W. Fairall, and S. A. Michelson, 2011: Impact of sea-spray on the atmospheric surface layer. *Bound.-Layer Meteor.*, **140**, 361–381.
- Bister, M., and K. A. Emanuel, 1998: Dissipative heating and hurricane intensity. *Meteor. Atmos. Phys.*, **65**, 233–240, doi:10.1007/BF01030791.
- Black, P. G., and Coauthors, 2007: Air–sea exchange in hurricanes: Synthesis of observations from the coupled boundary layer air–sea transfer experiment. *Bull. Amer. Meteor. Soc.*, **88**, 357–374.

- Businger, S., and J. A. Businger, 2001: Viscous dissipation of turbulence kinetic energy in storms. *J. Atmos. Sci.*, **58**, 3793–3796.
- Clift, R., J. R. Grace, and M. E. Weber, 1978: *Bubbles, Drops, and Particles*. Academic Press, 400 pp.
- DeCosmo, J., K. B. Katsaros, S. D. Smith, R. J. Anderson, W. A. Oost, K. Bumke, and H. Chadwick, 1996: Air-sea exchange of water vapor and sensible heat: The Humidity Exchange Over the Sea (HEXOS) results. *J. Geophys. Res.*, **101** (C5), 12 001–12 016.
- Donelan, M., B. K. Haus, N. Reul, W. J. Plant, M. Stiassnie, H. C. Graber, O. B. Brown, and E. S. Saltzman, 2004: On the limiting aerodynamic roughness of the ocean in very strong winds. *Geophys. Res. Lett.*, **31**, L18306, doi:10.1029/2004GL019460.
- Drennan, W. M., J. A. Zhang, J. R. French, C. McCormick, and P. G. Black, 2007: Turbulent fluxes in the hurricane boundary layer. Part II: Latent heat flux. *J. Atmos. Sci.*, **64**, 1103–1115.
- Emanuel, K. A., 1995: Sensitivity of tropical cyclones to surface exchange coefficients and a revised steady-state model incorporating eye dynamics. *J. Atmos. Sci.*, **52**, 3969–3976.
- Fairall, C. W., J. D. Kepert, and G. J. Holland, 1994: The effect of sea spray on surface energy transports over the ocean. *Global Atmos. Ocean Syst.*, **2**, 121–142.
- , E. F. Bradley, D. P. Rogers, J. B. Edson, and G. S. Young, 1996: Bulk parameterization of air-sea fluxes for Tropical Ocean-Global Atmosphere Coupled-Ocean Atmosphere Response Experiment. *J. Geophys. Res.*, **101** (C2), 3747–3764.
- , M. L. Banner, W. L. Peirson, W. Asher, and R. P. Morison, 2009: Investigation of the physical scaling of sea spray spume droplet production. *J. Geophys. Res.*, **114**, C10001, doi:10.1029/2008JC004918.
- Haus, B. K., D. Jeong, M. A. Donelan, J. A. Zhang, and I. Savelyev, 2010: Relative rates of sea-air heat transfer and frictional drag in very high winds. *Geophys. Res. Lett.*, **37**, L07802, doi:10.1029/2009GL042206.
- Jeong, D., B. K. Haus, and M. A. Donelan, 2012: Enthalpy transfer across the air–water interface in high winds including spray. *J. Atmos. Sci.*, **69**, 2733–2748.
- Joly, A., and Coauthors, 1997: The Fronts and Atlantic Storm-Track Experiment (FASTEX): Scientific objectives and experimental design. *Bull. Amer. Meteor. Soc.*, **78**, 1917–1940.
- Makin, V. K., 1998: Air-sea exchange of heat in the presence of wind waves and spray. *J. Geophys. Res.*, **103** (C1), 1137–1152.
- Mellado, J. P., 2010: The evaporatively driven cloud-top mixing layer. *J. Fluid Mech.*, **660**, 5–36, doi:10.1017/S0022112010002831.
- Mueller, J. A., and F. Veron, 2009: A sea state-dependent spume generation function. *J. Phys. Oceanogr.*, **39**, 2363–2372.
- NOAA Science Advisory Board, 2006: Majority report. Hurricane Intensity Research Working Group Majority Rep., 66 pp. [Available online at http://www.sab.noaa.gov/Reports/HIRWG_final73.pdf.]
- Ranz, W. E., and W. R. Marshall Jr., 1952: Evaporation from drops. *Chem. Eng. Prog.*, **48**, 141–146.
- Richter, D. H., and P. P. Sullivan, 2013a: Momentum transfer in a turbulent, particle-laden Couette flow. *Phys. Fluids*, **25**, 053304, doi:10.1063/1.4804391.
- , and —, 2013b: Sea surface drag and the role of spray. *Geophys. Res. Lett.*, **40**, 656–660, doi:10.1002/grl.50163.
- Rouson, D., and J. Eaton, 2001: On the preferential concentration of solid particles in turbulent channel flow. *J. Fluid Mech.*, **428**, 149–169.
- Spalart, P. R., R. D. Moser, and M. M. Rogers, 1991: Spectral methods for the Navier-Stokes equations with one infinite and two periodic directions. *J. Comput. Phys.*, **96**, 297–324.
- Zhang, J. A., P. G. Black, J. R. French, and W. M. Drennan, 2008: First direct measurements of enthalpy flux in the hurricane boundary layer: The CBLAST results. *Geophys. Res. Lett.*, **35**, L14813, doi:10.1029/2008GL034374.